Silicon
https://doi.org/10.1007/s12633-022-02081-z

ORIGINAL PAPER

Mixed-Mode Optical/Electric Simulation of Silicon Lateral PIN Photodiode Using FDTD Method

Samir Labiod[1,2] · Billel Smaani[2,3] · Shubham Tayal[4] · Shiromani Balmukund Rahi[5] · Hichem Sedrati[6] · Saida Latreche[2]

Received: 2 February 2022 / Accepted: 13 August 2022

Abstract
Within this paper, a total optoelectronic simulation of a PIN photodiode structure was presented. The microlens structure has been introduced on the top of the PIN photodiode to compensate the low sensitivity level of the sensor. Finite-Difference Time-Domain (FDTD) method has been used to estimate the optical generation inside the active device. Optical simulation was combined to the electric device simulation stemmed from the drift-diffusion model (DDM) that describe the charge carrier transport in the PIN photodiode. The suggested algorithm provides the time and space distribution of the principals parameters as carriers' concentration, electrostatic potential and current density. Furthermore, external quantum efficiency and sensitivity of the PIN photodiode are estimated and compared with the solution obtained from SILVACO-TCAD simulator.

Keywords FDTD method · Drift-diffusion model · Absorbing medium · Lateral PIN photodiode

1 Introduction

Recently, silicon PIN photo-detector has been drawing more and more attentions. It has been known to be able to rise transient time and reduce the junction capacitance, where intrinsic region is expanded to gain higher efficiency and photons generate further electron-hole pairs [1].

The speediness of a photodiode is based upon junction capacitance, drift, and diffusion. The drift time may be minimized by growing up the intrinsic breadth of the junction. The capacitance of the junction corresponds inversely to the length of the depletion region which can absorb more photons.

Compared to different optical detectors, PIN photodiode has different advantages, such as lower cost, smaller size and better resolution. PIN photodiode has been employed in multiple applications such as image sensing and computing the position of light.

PIN photodiode has high bandwidth at small bias voltage that makes it suitable for use in optical fiber communications and also for high-speed photometry [2].

The performance of light sensitive PIN photodiode can be improved by influencing the optical intensity

✉ Samir Labiod
s.labiod@univ-skikda.dz

Billel Smaani
billel.smaani@gmail.com

Shubham Tayal
shubhamtayal999@gmail.com

Shiromani Balmukund Rahi
sbrahivlsi@gmail.com

Hichem Sedrati
h.sedrati@univ-skikda.dz

Saida Latreche
latreche.saida@gmail.com

[1] Department of Physics, Faculty of Sciences, Université 20 Août 1955, BP 26 Route El-Hadaïk, 21000 Skikda, Algeria

[2] Laboratoire Hyperfréquences et Semiconducteurs, Université des frères Mentouri Constantine1, Constantine, Algeria

[3] Centre Universitaire Abdel Hafid Boussouf, Mila, Algeria

[4] SR University, Warangal, Telangana, India

[5] Department of Electrical Engineering, Indian Institute of Technology Kanpur, Kanpur 208016, India

[6] Laboratoire d'Anticorrosion, Matériaux Et Structure (LAMES), Faculté des Sciences, Université 20 Août 1955, BP 26 Route El-Hadaïk, 21000 Skikda, Algeria

Published online: 09 September 2022

distribution inside the structure considering optical and geometric characteristics such as lenses, antireflective coatings, absorbing regions.

Many publications introduce the rigorous electromagnetic wave propagation effects with electric active device modeling affecting the light sensitive devices and miniature microwave devices [3–5].

Different works have been carried out concerning this component. Huang et al. [6], carried out InGaN PIN photodiode that present a responsivity of 0.19 A/W at 402 nm for a zero-bias. However LU Yi-dan et al. [7] announced that this component displayed an unbiased responsivity of *0.22 A/W* at *378 nm*. Also, Totsuka et al. [8] reported that the proposed component can reach a responsivity of *0.34 A/W* for a 590 nm optical wavelength.

In this work, we propose a numerical model to simulate photo-detection in PIN photodiode using FDTD method [9].

The optical simulation model couples a two-dimensional (2-D) time-domain solution of Maxwell's equations to the active device model. The proposed model is qualified to report the electromagnetic wave propagation inside the PIN photodiode and to describe the interchange with an absorbing semiconductor medium.

The proposed active device is founded on the drift diffusion model equations which consider carrier's transport and Shockley–Read–Hall (SRH) model [10, 11]. This model can be simply derived from the Boltzmann equation (BTE) by considering some estimations and simplification.

To simulate such semiconductor photo-detector with complicated optical geometry, a various modeling technique is intended. Two-dimensional finite-difference algorithm (2D-FD) is proposed to simulate the PIN photodiode, also a full implicit scheme algorithm has been proposed to accomplish time domain. The obtained matrix systems are coupled by three unknowns, this problem is solved by using an efficient and specific algorithm based on the well-known Scharfetter-Gummel scheme [12, 13].

All numerical algorithms are easily programmable at the high level language for execution. The selected implementation language is MATLAB for its facility of use.

Table 1 summarizes the main performance of the proposed PIN photodiode and comparison with recently published photodiodes in Silicon based technology. Compared with other published photodiode, the PIN photodiode proposed in this work achieved a high quantum efficiency, good responsivity and low bias voltage meanwhile other key parameters are also competitive.

2 Electromagnetic Modeling of Light Propagation

To simulate the light propagation inside the active device, we will establish the Maxwell's equations for a PML (Perfectly Matched Layer) medium to avoid any optical reflections at boundaries [20, 21].

The 2D-Maxwell's equations in an absorbing medium for the transverse magnetic (TM) mode propagation are:

$$\begin{aligned}
&\varepsilon_0\varepsilon_r\frac{\partial E_z(x,y)}{\partial t}+\sigma E_z(x,y)=\frac{\partial H_y(x,y)}{\partial x}-\frac{\partial H_x(x,y)}{\partial y}\\
&\mu\frac{\partial H_x(x,y)}{\partial t}+\sigma_m H_x(x,y)=-\frac{\partial E_z(x,y)}{\partial y}\\
&\mu\frac{\partial H_y(x,y)}{\partial t}+\sigma_m H_y(x,y)=\frac{\partial E_z(x,y)}{\partial x}
\end{aligned}\tag{1}$$

where E_z is the electric component, $H=(H_x,H_y)$ is the magnetic field, μ is the permeability constant and ε_0 is the permittivity in vacuum. The considered medium has an electric conductivity σ and a magnetic conductivity σ_m. If $\sigma\neq 0$ and $\sigma_m\neq 0$, the system of Eq. (1) reduces to the Maxwell equations of the absorbing medium.

The relative permittivity ε_r is related to the refractive index n by [22]:

$$\varepsilon=\varepsilon_0 n^2 \tag{2}$$

In the cases where a frequency domain expression of these quantities are given, complex values of both n and ε are allowable, with the imaginary part indicating the attenuation of field in the material [23].

Table 1 Performance summary and comparison with recently published photodiodes

References	Device	Responsivity peak (A/W)	Quantum efficiency (%)	Wavelength at peak (μm)	Reverse bias (V)	Thermal stability(K)
[14]	Schottky	0.093	42.5	0.27	−15	–
[15]	Schottky	0.115	50	0.285	0	200
[16]	PIN	0.096	44.4	0.27	0	175
[17]	PIN	0.168	71	0.292	0	300
[18]	PIN	0.436	66	0.82	−5	300
[19]	PIN	0.65	65	0.5	−0.8	273
This work	PIN	0.435	79.31	0.71	−2	300

$$\begin{cases} n = \mathrm{Re}(n) + i\,\mathrm{Im}(n) \\ \varepsilon_r = \mathrm{Re}\left(\varepsilon_r\right) + i\,\mathrm{Im}\left(\varepsilon_r\right) \end{cases} \tag{3}$$

The time-harmonic version of Maxwell-Ampere equation states that:

$$\vec{\nabla} \times \vec{H} = \sigma \vec{E} - i\omega\varepsilon_0\,\mathrm{Re}\left(\varepsilon_r\right)\vec{E} \tag{4}$$

where ω is the angular frequency.

Equation (4), can be reformulated as follow:

$$\vec{\nabla} \times \vec{H} = -i\omega\left(\varepsilon_0\,\mathrm{Re}\left(\varepsilon_r\right) + i\frac{\sigma}{\omega}\right)\vec{E} \tag{5}$$

Hence

$$\varepsilon = \varepsilon_0\,\mathrm{Re}\left(\varepsilon_r\right) + i\frac{\sigma}{\omega} \tag{6}$$

Substituting Eq. (3) into (2), we get the complex permittivity as:

$$\varepsilon = \varepsilon_0\left[\left(\mathrm{Re}\,(n)^2 - \mathrm{Im}\,(n)^2\right) + i(2\,\mathrm{Re}(n)\,\mathrm{Im}(n))\right] \tag{7}$$

By identification between Eqs. (6) and (7), we can derive the conductivity expression:

$$\sigma = \frac{4\pi c_0 \varepsilon_0\,\mathrm{Re}(n)\,\mathrm{Im}(n)}{\lambda_0} \tag{8}$$

where c_0 is the velocity of light in vacuum and λ_0 is the wavelength of light.

2.1 Optical Modeling Using FDTD Method

The simulation space is supposed to be filled with a number of Yee cells. Every Yee cell is specified by the spatial and temporal discretization indices (i, j, k). The indices (i, j, k) are related to the physical space as $(x_i, y_j, t_k) = (i\,\Delta x, j\Delta y, k\Delta t)$, where Δx and Δy are the space increment and Δt is the time increment. Equation (1) are discretized using Yee's central differencing in both space and time. The expressions for the first partial space derivatives of E and H, evaluated at $t = k$. Δt, are given by:

$$H_x^{k+\frac{1}{2}}\left(i, j+\frac{1}{2}\right) = \frac{\mu - 0.5\,\Delta t\,\sigma_m}{\mu + 0.5\,\Delta t\,\sigma_m} H_x^{k-\frac{1}{2}}\left(i, j+\frac{1}{2}\right) - \frac{\Delta t}{\Delta y\,(\mu + 0.5\,\Delta t\,\sigma_m)}\left(E_z^k(i, j+1) - E_z^k(i, j)\right) \tag{9}$$

$$H_y^{k+\frac{1}{2}}\left(i+\frac{1}{2}, j\right) = \frac{\mu - 0.5\,\Delta t\,\sigma_m}{\mu + 0.5\,\Delta t\,\sigma_m} H_y^{k-\frac{1}{2}}\left(i+\frac{1}{2}, j\right) + \frac{\Delta t}{\Delta x\,(\mu + 0.5\,\Delta t\,\sigma_m)}\left(E_z^k(i+1, j) - E_z^k(i, j)\right) \tag{10}$$

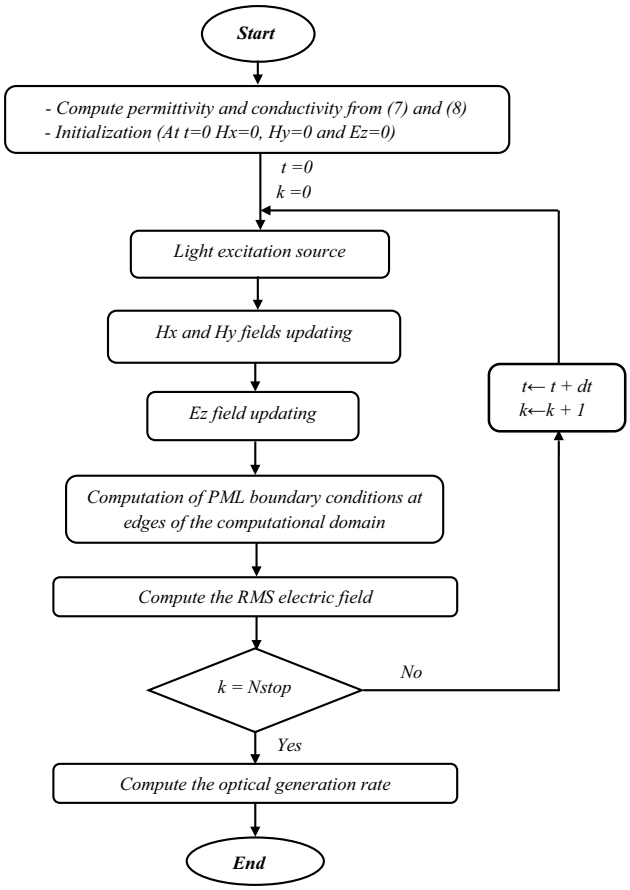

Fig. 1 Flowchart describing the sequence of operations to calculate the optical carrier generation

$$E_z^{k+1}(i,j) = \frac{\varepsilon - 0.5\,\Delta t\,\sigma}{\varepsilon + 0.5\,\Delta t\,\sigma} E_z^k(i,j) + \frac{\Delta t}{\Delta x\,(\varepsilon + 0.5\,\Delta t\,\sigma)}\left(H_y^{k+\frac{1}{2}}\left(i+\frac{1}{2}, j\right) - H_y^{k+\frac{1}{2}}\left(i-\frac{1}{2}, j\right)\right) - \frac{\Delta t}{\Delta y\,(\varepsilon + 0.5\,\Delta t\,\sigma)}\left(H_x^{k+\frac{1}{2}}\left(i, j+\frac{1}{2}\right) - H_x^{k+\frac{1}{2}}\left(i, j-\frac{1}{2}\right)\right) \tag{11}$$

The time step Δt is bounded by courant stability criterion, for more details and information we advise the reader to [24]. The conductivity σ is defined by Eq. (8).

The FDTD algorithm flow-chart to compute the lighting electromagnetic fields is composed by seven main modules, as shown in Fig. 1. In the FDTD algorithm, first, all matrix fields E_Z, H_x and H_y are defined in the initialization step (at t = 0 all fields are set to zero). The main parameters such as the permittivity and conductivity can be calculated from Eqs. (7) and (8), respectively.

At each grid point, the three finite-difference Eqs. (9), (10) and (11) are stepped in time alternately in order to update the electric and magnetic field components.

Moreover, at each time step, the lightning channel source is not included in the finite-difference equations for

the field components and therefore is applied separately. In this part of simulation a sinusoidal wave source of the form $\sin\left(\frac{2\pi c_0}{\lambda_0}t\right)$ is propagated in the desired direction. Boundary conditions are applied to avoid unwanted reflections of the electromagnetic field. These operations are repeated until the simulations are performed in the desired time period. The output of the FDTD algorithm would be the electric field at every observation point during the described time period. The electric field vary periodically with time, so the proposed algorithm compute the power density absorbed, which is given by the RMS (Root Mean Square) value of the electric field:

$$w = \frac{1}{2}\sigma|E|^2 \tag{12}$$

Using Eq. (12), optical carrier generation rate G is calculated using the following formula [23]:

$$G = \frac{w}{E_{ph}} \tag{13}$$

With the photon energy $E_{ph} = \frac{hc_0}{\lambda_0} = \hbar\omega$.

3 Active Device Model Formulation

The active device models used are generally obtained by applying estimations and simplification to the Boltzmann model. These simplifications can derive another transport model such as the drift diffusion model [25, 26].

The basic system of partial differential equations that explain the physical processes occurring in semiconductor devices.

The Poisson equation is stated as:

$$\nabla^2 V = \frac{q}{\varepsilon}(n - p - C) \tag{14}$$

Both of electron and hole continuity equations are given by:

$$\begin{aligned} \vec{\nabla}\vec{J}_n - q\frac{\partial n}{\partial t} &= q(R - G) \\ \vec{\nabla}\vec{J}_p + q\frac{\partial p}{\partial t} &= -q(R - G) \end{aligned} \tag{15}$$

where V correspond to the electrostatic potential, ε denotes the material permittivity, q is the elementary charge, $C = N_D^+ - N_A^-$ is the ionized impurity concentration, N_D^+ and N_A^- are the ionized donor and acceptor impurity distributions, respectively. The carriers current density are $\vec{J}_n = -q.n.\mu_n.\vec{\nabla}V + q.Dn.\vec{\nabla}n$ and $\vec{J}_p = -q.p.\mu_p.\vec{\nabla}V - q.Dp.\vec{\nabla}p$. Also, the diffusion coefficients are $D_n = \mu_n U_T$ and $D_p = \mu_p U_T$ of electrons and holes, respectively.

The validity of the drift-diffusion equations is empirically extended by introducing the electric field E and the ionized impurity concentration C dependent mobility μ [27].

$$\left(\frac{\mu_0}{\mu}\right)^2 = 1 + \left(\frac{C}{C/S + N}\right) + \left(\frac{(E/A)^2}{E/A + F}\right) + (E/B)^2 \tag{16}$$

The values of μ_0, N, S, A, F and B are presented in Table 2.

The Shockley–Read–Hall model of the carrier trap recombination are given by [28]:

$$R = \frac{n.p - n_i^2}{\tau_p.(n + n_i) + \tau_n.(p + n_i)} \tag{17}$$

with G denote the optical carrier generation rates. The carrier concentrations n and p are assumed to obey Maxwell-Boltzmann statistics:

$$\begin{cases} n = n_i \exp\left[(V - V_n)/U_T\right] \\ p = n_i \exp\left[(V_p - V)/U_T\right] \end{cases} \tag{18}$$

where $U_T = 0.026V$ is the thermal voltage, n_i is the effective intrinsic concentration (including heavy doping effects and band gap narrowing) and $V_{n,p}$ denote the respective Fermi potentials.

3.1 Electrical Boundary Conditions

Equation (14) are generally solved subject to a mixture of Dirichlet and homogeneous Neumann boundary conditions.

Dirichlet conditions for the potential V_B is defined by two values, the first is the externally applied to the contact V_A and the second is so called built-in-potential, which is produced by the doping

$$V_B = V_A + U_T \ln\left(\frac{N_D^+}{n_i}\right) \tag{19}$$

In the case where the contact surface is found at P region

$$V_B = V_A - U_T \ln\left(\frac{N_A^-}{n_i}\right) \tag{20}$$

Table 2 Constants values for the proposed mobility model

	μ_0(m^2/v.s)	N(At/cm^3)	S	A(v/m)	F	B(v/m)
Holes	480	4 10^{16}	81	6.1 10^3	1.6	2.5 10^4
Electrons	1400	3 10^{16}	350	3.5 10^3	8.8	7.4 10^3

Dirichlet conditions for carrier's densities n_B and p_B at contacts can be obtained by introducing thermal equilibrium and charge neutrality.

$$\begin{cases} n_B = \frac{1}{2}\left(N_D^+ + \sqrt{\left(N_D^+\right)^2 + \left(2n_i\right)^2}\right) \\ p_B = \frac{1}{2}\left(N_A^- + \sqrt{\left(N_A^-\right)^2 + \left(2n_i\right)^2}\right) \end{cases} \tag{21}$$

At the free edges of the device's simulation domain, homogeneous Neumann conditions are applied for the electrostatic potential and carrier densities.

$$\begin{cases} \frac{\partial V}{\partial N} = 0 \\ \frac{\partial n}{\partial N} = \frac{\partial p}{\partial N} = 0 \end{cases} \tag{22}$$

With N denoting the outward normal vector.

3.2 Solution of Coupled Poisson-Continuity System

Finite-difference method is applied for PIN photodiode by using Scharfetter-Gummel scheme as in [29], which consists in the computation of a sequence V^r, $r \geq 0$ with the new electrostatic potential V^{r+1} is deduced from the old electrostatic potential V^r by solving the following non-linear Poisson's Eq. (14), we get:

$$\nabla^2 V^{r+1} = \frac{q}{\varepsilon}(n^r + \Delta n - p^r - \Delta p - C) \tag{23}$$

new and old values of potential and carriers concentration are linked by $V^{r+1} = V^r + \Delta V$, $n^{r+1} = n^r + \Delta n$ and $p^{r+1} = p^r + \Delta p$.

From the equation system (18), the steps Δn and Δp are derived as follow:

$$\begin{cases} \Delta n = \frac{n}{U_T}\Delta V \\ \Delta p = -\frac{p}{U_T}\Delta V \end{cases} \tag{24}$$

By substituting Eq. (24) into Eq. (23), we get the Poisson's iterative equation as:

$$\nabla^2 V^{r+1} - \frac{q}{\varepsilon U_T}(p^r + n^r)V^{r+1} = \frac{q}{\varepsilon}(n^r - p^r - C) - \frac{q}{\varepsilon U_T}(p^r + n^r)V^r \tag{25}$$

By applying the standard first and second-order finite differences approximation to the spatial derivatives in Eq. (24), hence we obtain the linearized iterative finite difference final form,

$$\frac{1}{\Delta x^2}V_{i+1,j}^{r+1} + \frac{1}{\Delta x^2}V_{i-1,j}^{r+1} + \frac{1}{\Delta y^2}V_{i,j+1}^{r+1} + \frac{1}{\Delta y^2}V_{i,j-1}^{r+1} - \left[2\left(\frac{1}{\Delta y^2} + \frac{1}{\Delta x^2}\right) + \frac{q}{\varepsilon u_T}\left(n_{i,j}^r + p_{i,j}^r\right)\right].V_{i,j}^{r+1} = \frac{q}{\varepsilon}\left(n_{i,j}^r - p_{i,j}^r - C_{i,j}\right) - \frac{q}{\varepsilon u_T}\left(n_{i,j}^r + p_{i,j}^r\right)V_{i,j}^r \tag{26}$$

In this case, the space increments Δx and Δy are calibrated in order to satisfy Debye length criteria for semiconductor and optical wavelength simulation [30, 31].

The transient calculation is performed by simulating time-dependent of the drift-diffusion equations. The continuity Eq. (15) are discretized with a straightforward finite difference approach, the first order time derivative is approximated using finite difference Backward–Euler (BE) scheme [32].

The discretized electrons continuity equation lead to the five diagonal system:

$$\begin{aligned} &\frac{Dn_{i+\frac{1}{2},j}}{\Delta x^2}B\left(\frac{V_{i+1,j}^k - V_{i,j}^k}{u_T}\right)n_{i+1,j}^k + \frac{Dn_{i-\frac{1}{2},j}}{\Delta x^2}B\left(\frac{V_{i-1,j}^k - V_{i,j}^k}{u_T}\right)n_{i-1,j}^k + \frac{Dn_{i,j+\frac{1}{2}}}{\Delta y^2}B\left(\frac{V_{i,j+1}^k - V_{i,j}^k}{u_T}\right)n_{i,j+1}^k + \\ &\frac{Dn_{i,j-1/2}}{\Delta y^2}B\left(\frac{V_{i,j-1}^k - V_{i,j}^k}{u_T}\right)n_{i,j-1}^{r+1} - \left[\frac{Dn_{i+1/2,j}}{\Delta x^2}B\left(\frac{V_{i,j}^k - V_{i+1,j}^k}{u_T}\right) + \frac{Dn_{i-1/2,j}}{\Delta x^2}B\left(\frac{V_{i,j}^k - V_{i-1,j}^k}{u_T}\right)\right. \\ &\left. + \frac{Dn_{i,j+1/2}}{\Delta y^2}B\left(\frac{V_{i,j}^k - V_{i,j+1}^k}{u_T}\right) + \frac{Dn_{i,j-1/2}}{\Delta y^2}B\left(\frac{V_{i,j}^k - V_{i,j-1}^k}{u_T}\right) + \frac{1}{\Delta t}\right]n_{i,j}^k = R_{i,j}^{k-1} - G_{i,j} - \frac{1}{\Delta t}n_{i,j}^{k-1} \end{aligned} \tag{27}$$

where, $B(x) = \frac{x}{e^x - 1}$ is the Bernoulli's function. G is the optical generation calculated from the FDTD algorithm. The Shockley–Read–Hall carrier trap recombination $R_{i,j}^r$ presented in Eq. (17) is deduced from the old carrier concentration. The choice of the time step Δt is limited by the dielectric relaxation time [33].

A similar formula is obtained for the holes continuity equation:

$$\begin{aligned} &\frac{Dp_{i+1/2,j}}{\Delta x^2}B\left(\frac{V_{i,j}^k - V_{i+1,j}^k}{u_T}\right)p_{i+1,j}^k + \frac{Dp_{i-1/2,j}}{\Delta x^2}B\left(\frac{V_{i,j}^k - V_{i-1,j}^k}{u_T}\right)p_{i-1,j}^k + \frac{Dp_{i,j+1/2}}{\Delta y^2}B\left(\frac{V_{i,j}^k - V_{i,j+1}^k}{u_T}\right)p_{i,j+1}^k \\ &+ \frac{Dp_{i,j-1/2}}{\Delta y^2}B\left(\frac{V_{i,j}^k - V_{i,j-1}^k}{u_T}\right)p_{i,j-1}^k - \left[\frac{Dp_{i+1/2,j}}{\Delta x^2}B\left(\frac{V_{i+1,j}^k - V_{i,j}^k}{u_T}\right) + \frac{Dp_{i-1/2,j}}{\Delta x^2}B\left(\frac{V_{i-1,j}^k - V_{i,j}^k}{u_T}\right)\right. \\ &\left. + \frac{Dp_{i,j+1/2}}{\Delta y^2}B\left(\frac{V_{i,j+1}^k - V_{i,j}^k}{u_T}\right) + \frac{Dp_{i,j-1/2}}{\Delta y^2}B\left(\frac{V_{i,j-1}^k - V_{i,j}^k}{u_T}\right) + \frac{1}{\Delta t}\right]p_{i,j}^k = \left(R_{i,j}^{k-1} - G_{i,j}\right) - \frac{1}{\Delta t}p_{i,j}^{k-1} \end{aligned} \tag{28}$$

Both equation systems (27) and (28) can be used for the transient and steady state simulation. In order to obtain the steady state simulation, we set $n_{i,j}^k = n_{i,j}^{k-1}$ and $p_{i,j}^k = p_{i,j}^{k-1}$.

The three obtained steady state systems for Eqs. (26), (27) and (28) are solved in a decoupled manner with an efficient direct numerical LU decomposition method. The decoupled iteration solves Poisson's Eq. (26), initially with a guess for electrostatic potential, electrons and holes concentrations. The voltage distribution obtained is used to update the Bernoulli's and diffusion coefficients B, D_n and D_p followed by solving Eqs. (27) and (28) at all mesh points to provide new carrier concentration values and once again resolve Eq. (26), this procedure is repeated until the relative error in the potential norm is smaller than a fixed tolerance $\left\|\frac{V^{r+1} - V^r}{V^{r+1}}\right\| \leq \delta$. The generation recombination term depends on the carrier concentration, therefore it has to be updated at each iteration using the result for the electrons and holes concentrations.

Also, the whole numerical procedure outlines the calculation steps of the active device model for the steady state simulation is described as follows:

Begin

Step1: Compute optical carrier generation rates G using FDTD algorithm

Step2: Set potential, electron and hole boundary conditions based on equations (19)-(22)

Step3: Compute the initial guess for V, n and p vectors.

Do While $\left\| \frac{V^{r+1} - V^{r}}{V^{r+1}} \right\| \geq \delta$

Step4: Compute V by solving Eq (26)

Step5: Update generation recombination *R*

Step6: Update Bernoulli's coefficients *B*

Step7: Update diffusion coefficients D_n *and* D_p *using Eq (16)*

Step8: Compute n by solving Eq (27)

Step9: Compute p by solving Eq (28)

End do

Save *V*, *n* and *p*

Step9: Compute terminal current

End

The transient simulation requires the knowledge of the initial condition for electrostatic potential, electrons and holes vectors.

At each time index k, Bernoulli's coefficients are updated, then Eqs. (27) and (28) are resolved to obtain the electrons concentration n^{k+1} and holes concentration p^{k+1} for the next time index $k+1$, these concentrations are used to solve Poisson's Eq. (26) and compute the electrostatic potential V^{k+1} for the next time index $k+1$. This operation is repeated until the simulations are performed in the desired time period.

4 Results and Discussions

The 2-D structure used in this simulation is a vertical planar PIN photodiode with surface illumination as shown in Fig. 2. The SiO2 microlens is set on top of the active device. The length and the depth of the two doped regions are $a = 1.5\ \mu m$ and $h = 2\ \mu m$ respectively. The width of the intrinsic junction is $w = 2\ \mu m$. The height of the undoped substrate located below the structure is $s = 2\ \mu m$.

Concerning the optical part, the refractive index of the oxide is $n_{SiO2} = 1.5$, the front vertex of the microlens is $l = 2.1\ \mu m$ above the intrinsic region, the planar portion has a thickness of $t = 0.7\ \mu m$ and the aperture of the microlens is $d = 2.4\ \mu m$. A nitride layer is added between the oxide and silicon with thickness of $t_n = 0.15\ \mu m$, this layer acts as an antireflective coating.

Figure 3a and b presents the resulting doping profile at anode and cathode contacts. P and N regions ensure the ohmic contacts between conductors and device regions. The Gaussian profile distribution is used with a maximum density of 10^{17} At.cm^{-3} at anode and cathode contacts.

It's should be noted that the electrical simulations were performed at room temperature (T = 300 K).

4.1 Optical Simulation

The structure is illuminated with a plane, quasi-monochromatic, TM polarized wave incident from the top of the

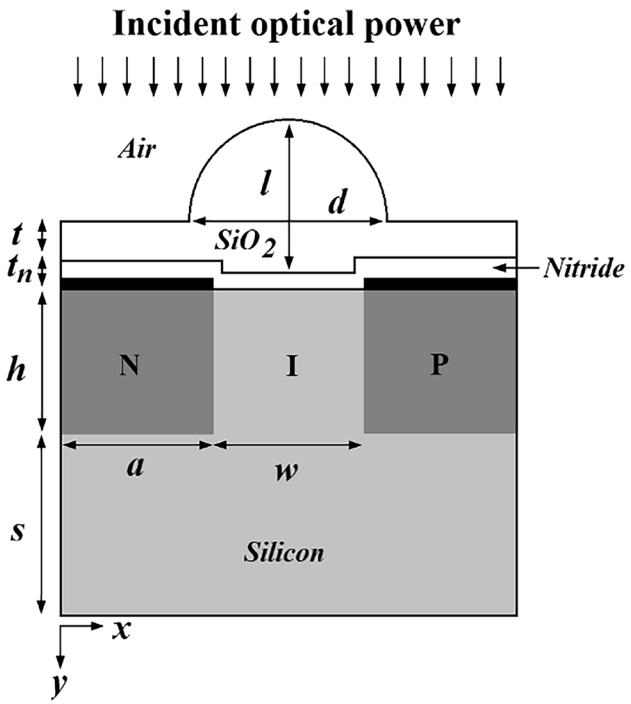

Fig. 2 The planar PIN photodiode structure

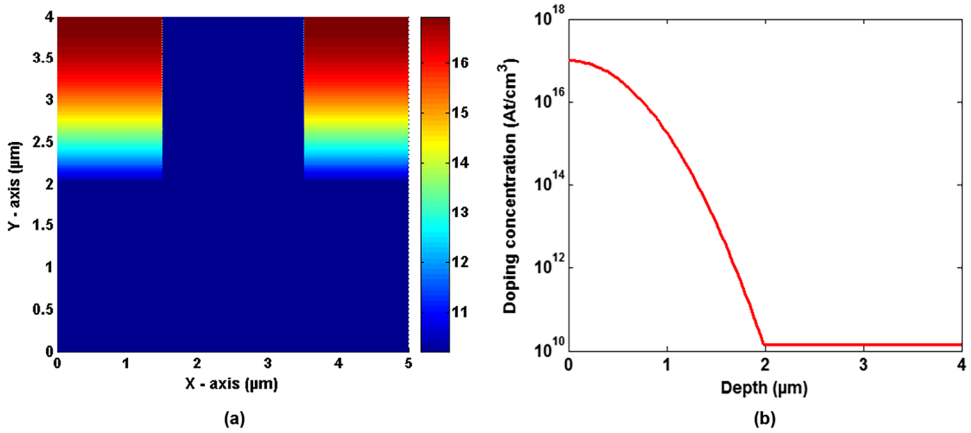

Fig. 3 Resulting doping profile in logarithmic scale: **a** 2D doping profile and **b** referenced 1D doping profile depth

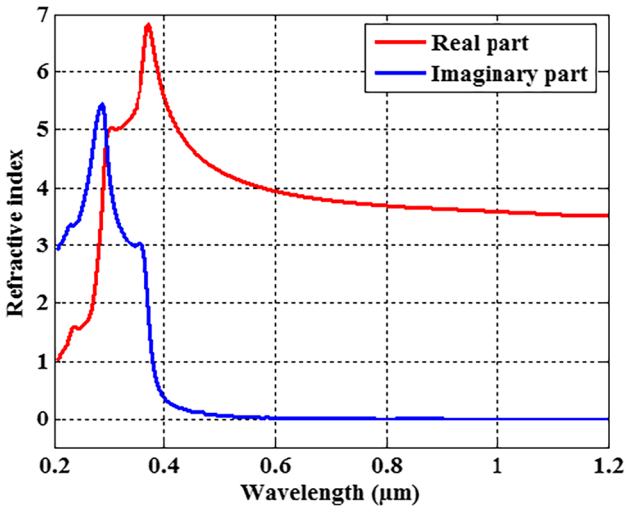

Fig. 4 Refractive index of silicon, variation of real and imaginary part with wavelength, reproduced from [34]

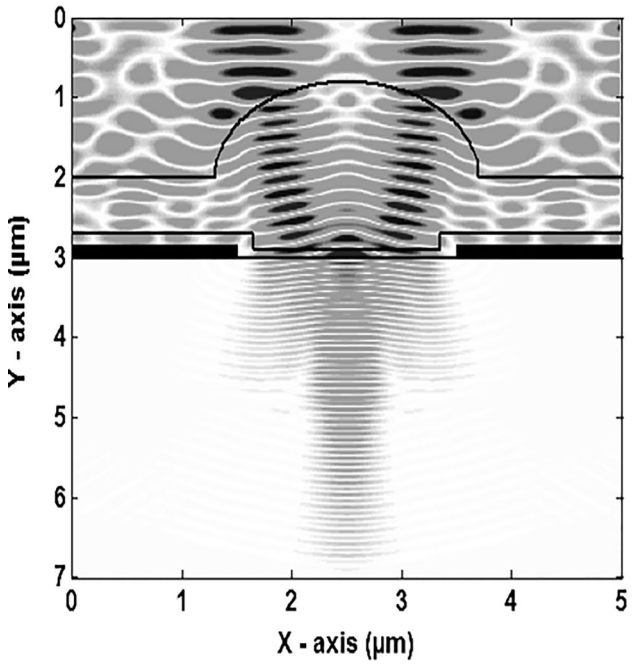

Fig. 5 Instantaneous intensity distribution in time harmonic state

structure. The optical source wavelength is *0.55 µm* and the power intensity of the light is *0.5 W/cm*^{2}.

In the FDTD simulation, the complete computational domain covered of 170 × 70 mesh nodes.The relative permittivity of the silicon is calculated from the refractive index for different incident wavelengths (Fig. 4).

Absorbing boundary condition is set at external boundaries to simulate a free space surrounding the structure. The shield metal of anode and cathode contacts was assumed to consist of a perfect electric conductor (PEC). Therefore, at metal boundaries we set the electric field tangential component to zero.

Figure 5 shows the instantaneous distribution profile of electromagnetic intensity in the considered geometry. It is shown that the electromagnetic field is more likely to be trapped outside the intrinsic layer for the wavelength *0.55 µm*. Also, we can see that the intensity of the electromagnetic wave becomes weak substantially deep inside the considered device, which proves the existence of the absorption effect in the Silicon material.

Figure 6 shows the resulting carrier generation rates distribution inside the device. The enhanced charge carrier generation is observed for PIN photodiode due to the stronger photon absorption eventually at the intrinsic region. Subsequently, the 2D generation rate data predicted by the FDTD algorithm is imported into the numerical electronic modelling that creates bridge between electromagnetic absorption and electric device simulation.

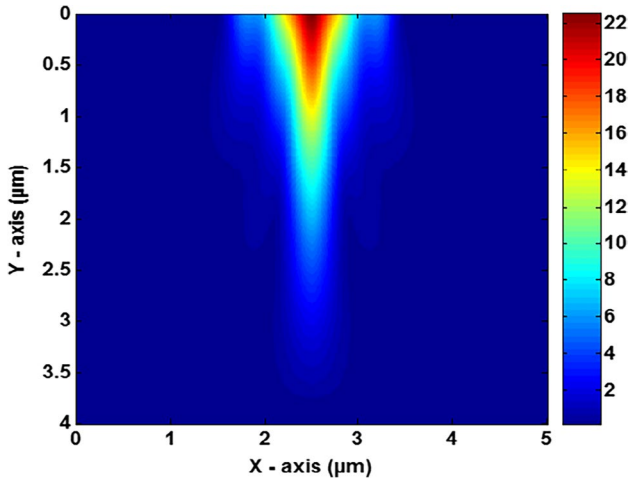

Fig. 6 Charge carrier generation rate for the proposed structure in logarithmic scale

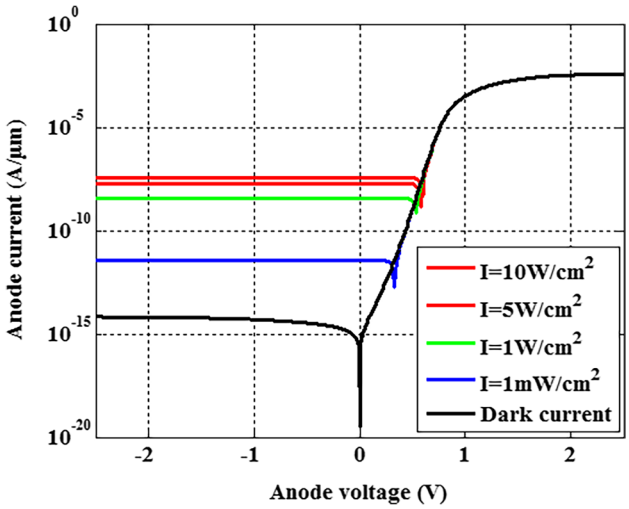

Fig. 8 Calculated I–V characteristics by varying optical power intensity

4.2 Steady-State Simulations

Including the optical illumination, the steady-state solution for carrier concentrations and I-V characteristics are calculated. The electrons and holes distributions are illustrated in Fig. 7a and b respectively. We can see the appearance of both electron and hole in a symmetrical way, which reduce the resistivity of the intrinsic layer between anode/cathode junctions.

In order to calculate the current variation with potential, the simulation was performed by varying cathode voltage from −2.3 to 2.5 V in 0.05 steps. At each voltage value, cathode current is calculated by integrating current density over cathode contact.

To analyze the charge transport and photo-conducting mechanisms of the PIN photodiode, Fig. 8 demonstrate the I-V characteristics in logarithmic scale for various illumination intensities. As shown in Fig. 8, the optical current is strongly related to the increasing of the optical power intensity, and still constant with anode voltage. Also, whenever the optical power intensity is high, the optical current becomes important in the forward bias region. In other words, the optical current can be obtained for direct biases, but for a restricted interval. For the optical power intensities $1\,mW/cm^2$ and $10W/cm^2$, the optical current remains constant even for the positive voltage values *0.28 V* and *0.58 V* respectively. Without optical radiation, the dark current is relatively very small ~6.7 10^{-15}A and exist only for the reverse bias case.

4.3 Time-Depend Simulations

In this case of simulation, the device is biased with 2 V of reverse potential. Figure 9 shows the reversible switching between high and low conductance when the illumination is turned on, the pulsed light were performed under illumination light intensity of $1\ mW/cm^2$ at wavelength $\lambda = 0.55\ \mu m$.

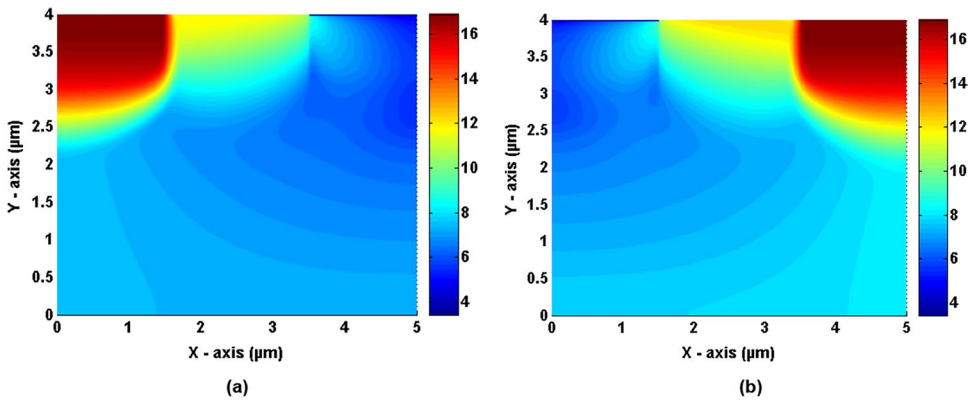

Fig. 7 Carrier concentration inside PIN diode: **a** electron concentration and **b** hole concentration

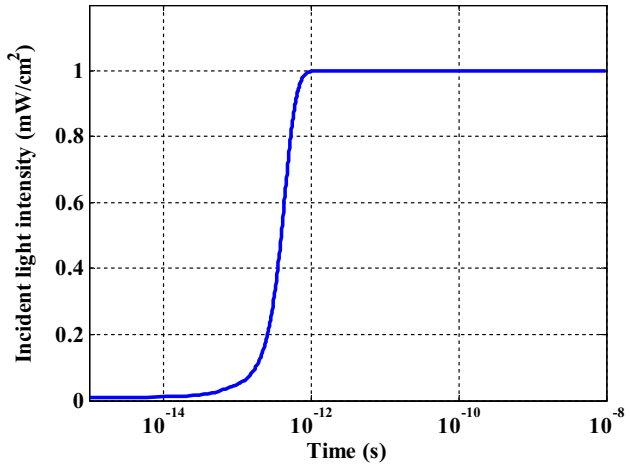

Fig. 9 Applied light intensity versus time

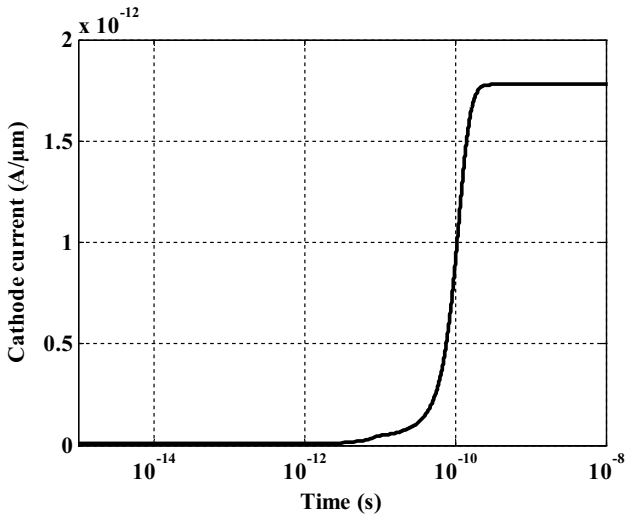

Fig. 10 Calculated transient current

The time-dependence of the cathode current in response to the optical power intensity is illustrated in Fig. 10. When the incident light intensity is switched, the cathode current shows a sudden increase but with little temporal shift. This temporal shift occurs because of the accumulation of electron-hole pairs in the intrinsic region requires a specific time. It has been found that the PIN photodiode is saturated after *0.29 ns* with a response time of *2.5 ps*. The obtained results clearly demonstrate that the computed current at steady-state are in well agreement with the expected value obtained by the stationary approach for the time depend simulation.

4.4 Spectral Simulation

The spectral simulation was carried out in the range of *0.2-1.2 µm* wavelength under a reverse potential of *2v* with an optical intensity of *0.5 W/cm*^{2}.

With the aim of calculating external quantum efficiency, at each wavelength step the external optical energy over the microlens and output steady-state photocurrent are calculated.

External quantum efficiency is presented in Fig. 11a, EQE of >50% is achieved for wavelengths ranging from *0.411* to *0.834 µm*. A maximum EQE of 79.31% is observed at 850 nm. This efficiency is assigned to the effective accumulation of charge carriers photo-generated in the intrinsic region of the PIN photodiode.

Figure 11b shows the calculated spectral sensitivity, it's clearly observed that the Silicon PIN photodiode produced a maximum sensitivity of *0.435 A/W* at a wavelength *0.71 µm*. It is apparent that at the edges of the wavelength range, the system had a poor production of free charge carriers (electron-hole pairs). And this poor production was due to front-rear surface recombination, thus reduced absorption at long and low wavelengths diffusion lengths. To validate the proposed numerical model, the same structure is simulated using the commercial simulator SILVACO-TCAD. The slight differences between the developed code and TCAD simulation outcomes can hence be ascribed to the different approaches followed to describe the

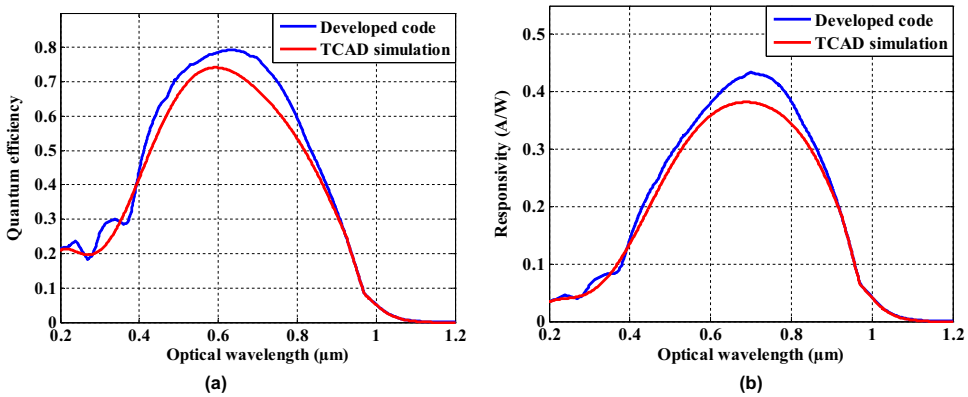

Fig. 11 Spectral results for silicon planar PIN photodiode: **a** external quantum efficiency and **b** responsivity

optical carrier generation rates and also the different approaches such as numerical method resolution. However, the accuracy is acceptable and the agreement remains good.

5 Conclusion

A combined optical and electric simulation of PIN photodiode structure design has been reached out for a range of illumination wavelengths.

First, we have proposed an efficient time-domain simulator for a rigorous simulation of the propagation of light in an absorbing medium.

In order to simulate the electric transport phenomena inside the active device, a two-dimensional time dependent simulator is developed to solve drift-diffusion model.

Steady state solutions are presented such as the space repartition of the carrier concentration and also the *I-V* characteristics of the PIN photodiode. Transient solutions describe the variation of the integrated electrons and terminal photocurrent versus time. The time reaction of the PIN photo-detector to light illumination is fast-varying. This feature makes it an important element to use in the optical-switch applications. In addition, spectral results have been calculated in the range of 0.2-1.2 µm, the quantum efficiency of PIN photodiodes increases up to 79.31% and the peak responsivity of devices is 0.435 at 0.71 µm. In summary, although the spectral characteristics are in good agreement with standard commercial software (SILVACO-TCAD). According to the obtained results, it is evident that the proposed device can be used as photo-detector. Finally, the presented numerical model in this work provides an interesting contribution to the active device photo-detectors. Also to rise the accuracy of this model, the proposed analysis can be extended to more complex geometries and more physical parameters.

Acknowledgments I would like to thank all authors who helped me to settle many problems that came up as the writing of this article. At last, we would like to thank everyone who helped and motivated us to work on this article.

Author Contributions All included authors in the research manuscript have equal contribution.

Data Availability Data and materials are original work of authors.

Declarations

The procedure followed in this work is in accordance with ethical standards. This article does not contain any studies with human participants or animals performed by any of the authors.

Consent to Participate None.

Consent for Publication None.

Conflict of Interest There is no conflict of interest from others.

References

1. Sze SM, Ng KK (2007) Physics of semiconductor devices. Wiley, Hoboken
2. Klinger S, Berroth M, Kaschel M, Oehme M, Kasper E (2009) Ge on Si p-i-n photodiodes with a 3-dB bandwidth of 49 GHz. IEEE Photon Technol Lett 21:920–922. https://doi.org/10.1109/LPT.2009.2020510
3. Satoh T, Mutoh N, Furumiya M, Murakami I, Suwazono S, Ogawa C, Hatano K, Utsumi H, Kawai S, Arai K, Morimoto M, Orihara K, Tamura T, Teranishi N, Hokari Y (1997) Optical limitations to cell size reduction in it-ccd image sensors. IEEE Trans Electron Devices 44:1599–1603. https://doi.org/10.1109/16.628810
4. Mutoh H (1997) Simulation for 3-D optical and electrical analysis of CCD. IEEE Trans Electron Devices 44:1604–1610. https://doi.org/10.1109/16.628811
5. Körner TO (2000) Combined optical and electric simulation of metal-semiconductor-metal photodetectors. IEE Proc-Optoelectron 147:89–95. https://doi.org/10.1049/ip-opt:20000293
6. Huang B, Jintong X, Wang L, Zhang Y, Li X (2017) Performance of back-illuminated $In_{0.09}$ $Ga_{0.91}$ N-based p–i–n photodetector. Opt Quant Electron 49:138. https://doi.org/10.1007/s11082-017-0970-2
7. Lu Y, Zhang Y, Li XY (2014) Properties of InGaN P-I-N ultraviolet detector. 7th international symposium on advanced optical manufacturing and testing technologies, optoelectronics materials and devices for sensing and imaging, 92840P. https://doi.org/10.1117/12.2073317
8. Totsuka D, Yanagida T, Fukuda K, Kawaguchi N, Fujimoto Y, Pejchal J, Yokota Y, Yoshikawa A (2011) Performance test of Si PIN photodiode line scanner for thermal neutron detection. Nucl Instrum Methods Phys Res 659:399–402. https://doi.org/10.1016/j.nima.2011.08.014
9. Yee KS (1966) Numerical solution of initial boundary value problems involving Maxwell's equations in isotropic media. IEEE Trans Antennas Propag 14:302–307. https://doi.org/10.1109/TAP.1966.1138693
10. Shockley W, Read WT (1952) Statistics of the recombinations of holes and electrons. Phys Rev 87:835–842. https://doi.org/10.1103/PhysRev.87.835
11. Hall RN (1952) Electron-hole recombination in germanium. Phys Rev 87:387–387. https://doi.org/10.1103/PhysRev.87.387
12. Gummel HK (1964) A self-consistent iterative scheme for one-dimensional steady state transistor calculation. IEEE Trans Electron Devices 11:455–465. https://doi.org/10.1109/T-ED.1964.15364
13. Schafetter DL, Gummel HK (1969) Large-signal analysis of a silicon read diode oscillator. IEEE Trans Electron Devices 16:64–77. https://doi.org/10.1109/T-ED.1969.16566
14. Lioliou G, Mazzillo MC, Sciuto A, Barnett AM (2015) Electrical and ultraviolet characterization of 4H-SiC Schottky photodiodes. Opt Express 23:21657–21670. https://doi.org/10.1364/OE.23.021657
15. Xu Y, Zhou D, Lu H, Chen D, Ren F, Zhang R, Zheng Y (2015) High-temperature and reliability performance of 4H-SiC Schottky-barrier photodiodes for UV detection. J Vac Sci Technol B 33:040602. https://doi.org/10.1116/1.4923083
16. Yang S, Zhou D, Lu H, Chen D, Ren F, Zhang R, Zheng Y (2016) High-performance 4H-SiC pin ultraviolet photodiode with p layer formed by al implantation. IEEE Photon Technol Lett 28:1189–1192. https://doi.org/10.1109/LPT.2016.2535407
17. Rao S, Mallemace ED, Della Corte FG (2022) High- performance 4H-SiC UV p-i-n photodiode: numerical simulations and experimental results. Electronics 11:1839. https://doi.org/10.3390/electronics11121839

18. Doğanci E, Kaya Ş, Aktağ A, Sarigül Duman E, Turan R, Karaçali H, Yilmaz E (2019) Fabrication and characterization of Si-PIN photodiodes. Turk J Phys 43:556–562. https://doi.org/10.3906/fiz-1905-16
19. Kundu A, Adhikari S, Das A, Kanjilal M, Mukherjee M (2018) Design and characterization of asymetrical super-lattice Si/4H-SiC pin photo diode array: a potential opto-sensor for future applications in bio-medical domain. Microsyst Technol 27:569–584. https://doi.org/10.1007/s00542-018-4119-4
20. Berenger JP (1996) Perfectly matched layer for the FDTD solution of wave-sturcture interaction problems. IEEE Trans Antennas Propag 44:110–117. https://doi.org/10.1109/8.477535
21. Berenger JP (1994) A perfectly matched layer for the absorption of electromagnetic waves. J Comput Phys 114:185–200. https://doi.org/10.1006/jcph.1994.1159
22. Chen LF, Ong CK, Neo CP, Varadan VV, Varadan VK (2004) Microwave electronics: measurement and materials characterization. Wiley
23. Körner TO, Gull R (2000) Combined optical/electric simulation of CCD cell structures by means of the finite-difference time-domain method. IEEE Trans Electron Devices 47:931–938. https://doi.org/10.1109/16.841223
24. Taflove A, Hagness S (2005) Computational electrodynamics: the finite-difference time–domain method3rd edn. Artech House
25. Vasileska D, Goodnick SM (2006) Computational electronics. Morgan and Claypool Publishers
26. Smaani B, Rahi SB, Labiod S (2022) Analytical compact model of nanowire junctionless gate-all-around MOSFET implemented in verilog-a for circuit simulation. Silicon. https://doi.org/10.1007/s12633-022-01847-9
27. Labiod S, Latreche S, Gontrand C (2012) Numerical modeling of MOS transistor with interconnections using lumped element-FDTD method. Microelectron J 43:955–1002. https://doi.org/10.1016/j.mejo.2012.10.005
28. Palankovski V, Quay R (2004) Analysis and simulation of heterostructure devices. Springer, Wien
29. Zhimeng T, Ye H, Qinyi T (1994) Generalized Scharfetter-Gummel scheme reducing the crosswind effect for the current continuity equation including energy balance. Comput Phys Commun 79:190–200. https://doi.org/10.1016/0010-4655(94)90067-1
30. Aste A, Vahldieck R (2003) Time-domain simulation of the full hydrodynamic model. Int J Numer Model Electron Netw Devices Fields 16:161–174. https://doi.org/10.1002/jnm.491
31. Vasileska D, Goodnick SM, Klimeck G (2010) Computational electronics, Semiclassical and quantum device modeling and simulation, 1st edn. CRC Press, Boca Raton
32. Sadiku MNO (2009) Numerical techniques in electromagnetic with matlab, 3rd edn. CRC press, Boca Raton
33. Bank RE, Coughran WM, Fichtner W, Grosse EH, Rose DJ, Smith RK (1985) Transient simulation of silicon devices and circuits. IEEE Trans Computer-Aided Design 4:436–451. https://doi.org/10.1109/TCAD.1985.1270142
34. Aspnes DE, Studna AA (1983) Dielectric functions and optical parameters of Si, Ge, GaP, GaAs, GaSb, InP, InAs, and InSb from 1.5 to 6.0 eV. Phys Rev B 27:985–1009. https://doi.org/10.1103/PhysRevB.27.985